Pulse pile-up recovery for the front-end electronics of the PANDA Electromagnetic Calorimeter

Tambave, G.; Kavatsyuk, M.; Guliyev, E.; Schreuder, F.; Moeini, H.; Löhner, H.

Published in:
Journal of Instrumentation

DOI:
10.1088/1748-0221/7/11/P11001

Publication date:
2012

Journal of Instrumentation

SISSA

OPEN ACCESS

Pulse pile-up recovery for the front-end electronics of the PANDA Electromagnetic Calorimeter

To cite this article: G Tambave *et al* 2012 *JINST* **7** P11001

PUBLISHED BY IOP PUBLISHING FOR SISSA MEDIALAB

RECEIVED: *August 2, 2012*
REVISED: *September 20, 2012*
ACCEPTED: *October 7, 2012*
PUBLISHED: *November 5, 2012*

Pulse pile-up recovery for the front-end electronics of the PANDA Electromagnetic Calorimeter

G. Tambave,[a,1] **M. Kavatsyuk,**[a] **E. Guliyev,**[a,b] **F. Schreuder,**[a] **H. Moeini**[a] **and H. Löhner**[a]

[a]*Kernfysisch Versneller Instituut,*
Zernikelaan 25, NL-9747 AA, Groningen, The Netherlands
[b]*Laboratoire Leprince-Ringuet,*
Ecole polytechnique, 91128, PALAISEAU Cedex, France

E-mail: g.j.tambave@rug.nl

ABSTRACT: At the future Facility for Antiproton and Ion Research near Darmstadt in Germany the PANDA detector will be employed to study the charmonium spectrum and to search for narrow exotic hadronic states, predicted by Quantum Chromodynamics. In the PANDA experiment, 1.5 to 15 GeV/c anti-protons will annihilate with a hydrogen target at an average rate of 20 MHz. Among the sub-detectors of PANDA is the Electromagnetic Calorimeter (EMC) planned for the studies of electromagnetic transitions and neutral meson decays. Due to the high annihilation rates, the EMC will be exposed to single-detector hit rates up to 500 kHz, which may lead to pulse overlap. Hence, to recover the energy and time information of the overlapping pulses, a pulse pile-up recovery method is developed. The method is easy to implement in FPGA for online data processing. The Constant Fraction Timing algorithm is applied at the trailing edge to determine the time stamp of pile-up pulses. The energy and the time information of pile-up pulses can be recovered up to time differences of 50 ns, equal to the pulse rise-time, in a large dynamic energy range.

KEYWORDS: Data processing methods; Digital signal processing (DSP); Calorimeters

[1]Corresponding author.

doi:10.1088/1748-0221/7/11/P11001

2012 JINST 7 P11001

Contents

2012 JINST 7 P11001

1 Introduction

The PANDA experiment [1] at the FAIR facility [2] near Darmstadt, Germany, will study antiproton-proton annihilations in order to test the validity of QCD at the long-distance scale. The experiment aims to search for predicted exotic hybrid and glue-ball states using high-resolution meson spectroscopy. In order to reconstruct hybrid and glue-ball states from their multi-photon and charged particle final states, high resolution calorimetry is required. The PANDA Electromagnetic Calorimeter (EMC) [3] has been designed to provide high energy and time resolution of about 2.5% at 1 GeV and ≤ 1 ns, respectively. The EMC has to cover a wide dynamic range of 10000 for the energy measurement, and has to be able to operate at high single-crystal hit-rates in the range of 0.5-1 MHz. The EMC is subdivided into three different parts, namely the forward endcap, backward endcap, and barrel EMC. Each part will have its dedicated readout electronics [4] adapted to the limitations imposed by space, power consumption, and detector pulse rate.

In the PANDA experiment, anti-protons with momenta between 1.5 and 15 GeV/c will interact with either a pellet or a cluster-jet hydrogen target at annihilation rates up to $2 \cdot 10^7$ events/s. Since PANDA is a fixed target experiment, hit rates up to 100 kHz are expected in the barrel EMC and more than 500 kHz in the forward endcap EMC. These high rates may lead to pulse overlap i.e. pile-up. The simulated hit-rate distribution [3] for the forward endcap EMC is shown in figure 1. The PANDA EMC trigger-less readout chain [4] is shown in figure 2. In the initial stage of the digitization process the shaped pile-up pulses will be identified and then transferred to the data

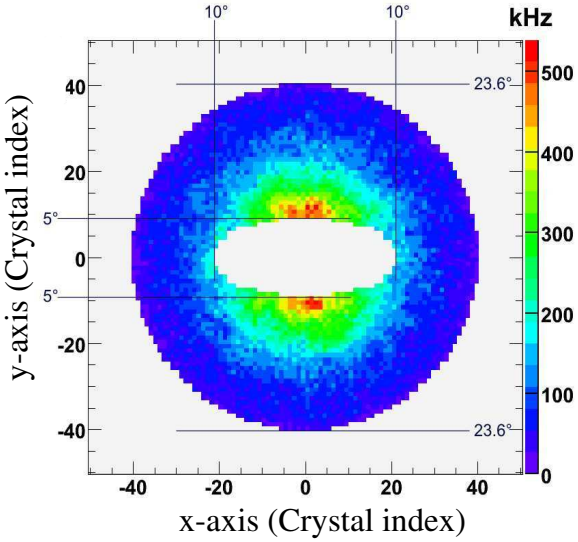

Figure 1. Integrated single-crystal hit rate [3] as function of vertical and horizontal coordinates for the forward endcap EMC simulated using the DPM (Dual Parton Model) generator at anti-proton beam momentum of 15 GeV/c. The hit rate is about 500 kHz at polar angle of about 5°.

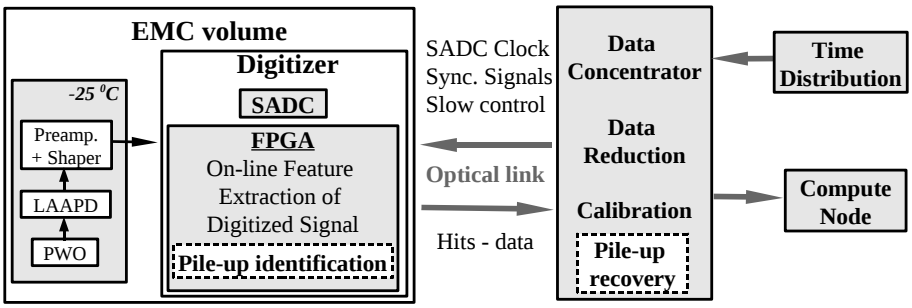

Figure 2. Schematic representation of the PANDA EMC trigger-less readout chain.

concentrator where the pile-up recovery algorithm will be applied. The pile-up recovered information will be sent to the compute node for on-line clustering and shower energy reconstruction. The single-pulse feature-extraction algorithms have already been implemented in FPGA and tested successfully [5]. At present, the FPGA implementation of the algorithm is re-written in a pipelined way, which eliminates dead-time caused by the data processing. The only possible source of the dead-time of the system is pile-up of sequential pulses. In this work the pile-up pulse recovery algorithm is developed and tested offline on the LED light pulser data as well as on the simulated pile-up pulses over a large dynamic range. The implementation of the pile-up recovery algorithm in VHDL code for an FPGA is in progress. The offline tests reveal that the pile-up pulse recovery method can recover pile-up pulse information up to a minimum pulse distance of 50 ns keeping the dead-time of the readout chain below 50 ns. To deal with pile-up pulses, various methods have been introduced and developed [6–8]. Since the data for the PANDA EMC will be processed on-line in FPGAs, we are developing a FPGA-friendly method. The digitizer modules, which will process

2012 JINST 7 P11001

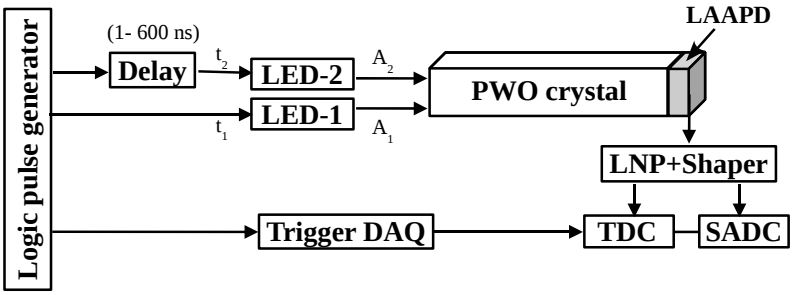

Figure 3. The block-diagram of the experimental setup. The details are explained in the text.

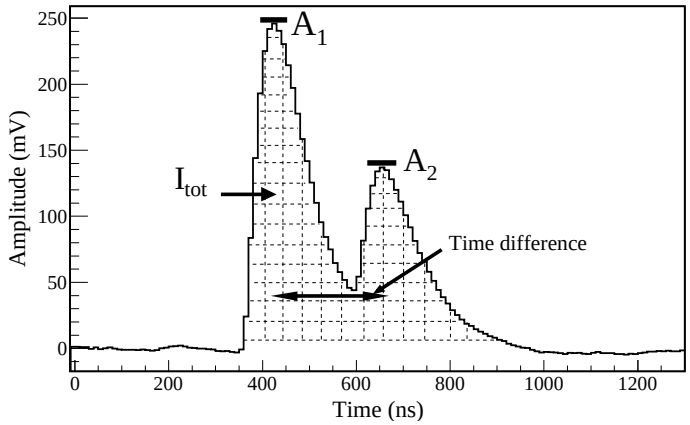

Figure 4. Digitized pile-up pulse waveform, generated by two LED light pulsers. The time difference ($\Delta\tau$) between the first and the second pulse is about 200 ns and the amplitude ratio is 2 (A_1/A_2 = 246 mV / 121 mV) where A_1 is the first, A_2 is the second pulse amplitude and I_{tot} is the integral of the pile-up pulse waveform.

data on-line, will be located inside the detector volume. This sets constraints on the power consumption. Therefore, the developed data processing algorithms have to consume as little resources as possible.

Due to the fluctuations in the hydrogen pellet target density [9] the peak hit rate at the forward endcap EMC will be 1 MHz resulting in pile-up rates up to 24% for the pulse width of 280 ns. By applying the proposed pile-up recovery method the pile-up rate is reduced to 4.2%. Also, at nominal hit rates of 500 kHz, the pile-up rate of 13% is reduced to 2.4%. The method was successfully tested for various combinations of amplitude ratios (pulse 1/ pulse 2). The energy and time of the pile-up pulses can be recovered up to time differences equal to the pulse rise-time.

2 Experimental setup

The block diagram of the electronics configuration used for systematic studies of pile-up events is shown in figure 3. The setup consists of a single $2 \times 2 \times 20$ cm^3 $PbWO_4$ (PWO) scintillating crystal kept at room temperature. A Large Area Avalanche Photodiode (LAAPD) photo sensor with gain of 200 was mounted on a 2×2 cm^2 face of the PWO crystal. The sensor was coupled to a LNP

2012 JINST 7 P11001

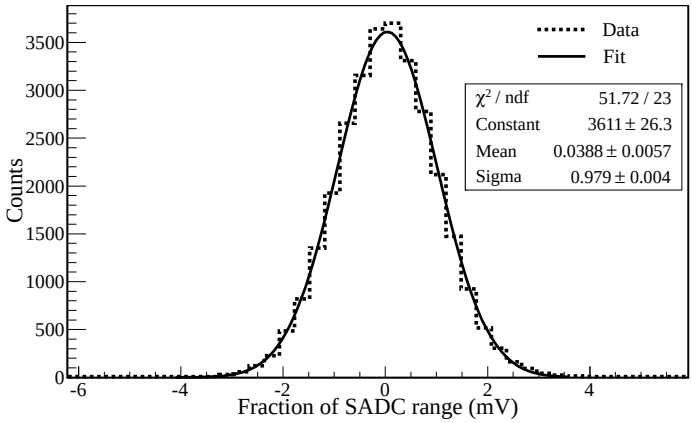

Figure 5. Baseline distribution of the digitized signal trace. The dashed line corresponds to the measured data and the solid line to the Gaussian fit. The width sigma obtained from the fit indicates the noise level of ~ 1 mV.

preamplifier [10] with four-stage analog shaper (dual gain, rise time 50 ns) feeding signals to a 16-bit 100 MHz Struck [11] Sampling ADC (SADC). Two LED light pulsers were used to generate double-pulses. The light pulse of the LED-2 was delayed using a variable delay line in order to generate pulse pile-up. The light was guided using a bundle of optical fibers, shining light on the face of the PWO crystal opposite to the LAAPD. In this setup the PWO crystal acts as waveguide. The LNP preamplifier converts the charge signal from the LAAPD to voltage pulses with a long exponential tail of 25 μs. The LNP pulses were further shaped using a four-stage analog shaper, resulting in the pulse width of 280 ns. The analog-shaper pulses were digitized by the SADC. Data were collected for various time differences $\Delta\tau$ by making a time scan of the delayed pulse over a time interval of 1 ns $< \Delta\tau <$ 600 ns for various pulse amplitudes A_1 and A_2. During the scan measurements the $\Delta\tau$ distribution was kept as close as possible to a uniform distribution. In addition to the SADC data, the reference time of the first (t_1) and the second (t_2) pulses were recorded by the time-to-digital converter (TDC). An example of a digitized pile-up pulse waveform for the time difference of 200 ns and the amplitude ratio of 2 ($A_1/A_2 = 246$ mV$/121$ mV) is shown in figure 4. Here, A_1 is the first and A_2 is the second pulse amplitude. The baseline distribution of the digitized signal trace is shown in figure 5. The width sigma obtained from the Gaussian fit indicates the noise level of ~ 1 mV.

3 Algorithm, results, and discussion

3.1 Pile-up pulse identification

As mentioned in section 1, the pulse pile-up identification takes place in the digitizer (figure 2) in the initial stage of the digitization process. For the identification process the following considerations are in order. The pile-up of two pulses happens when both pulses have amplitudes above the pulse-detection threshold and both pulses merge into a single structure extending above the threshold. The pile-up identification algorithm is based on the assumption of stability of the pulse shape in the complete dynamic range. For a stable pulse shape, the ratio of the incoming pulse Integral

2012 JINST 7 P11001

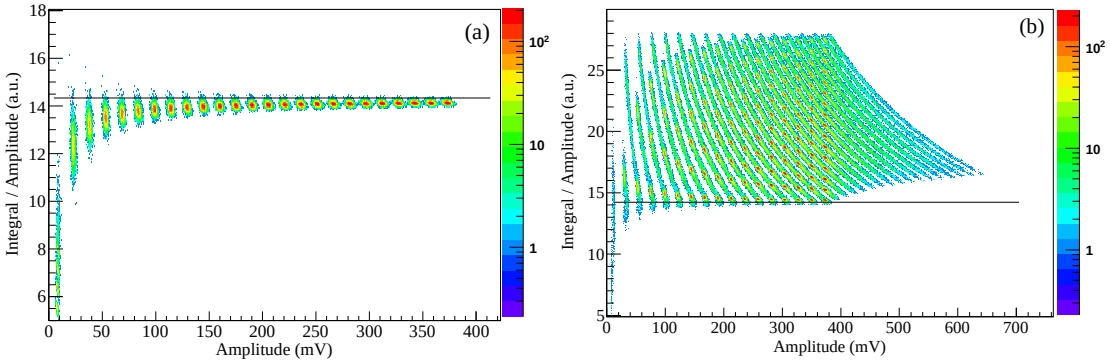

Figure 6. The ratio of the pulse integral over the pulse amplitude as function of the pulse amplitude from simulations: (a) for single pulses only; (b) for pile-up pulses only. Horizontal line indicates the pile-up identification threshold $T_{I/A} = 14.3$.

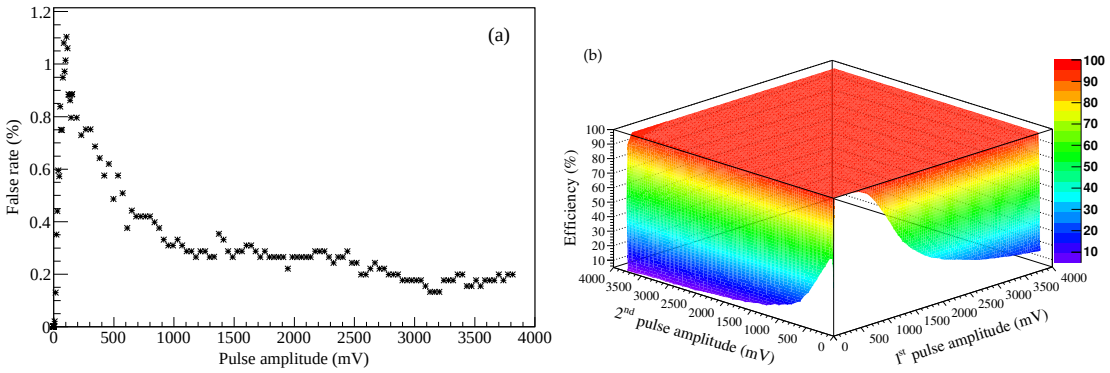

Figure 7. (a) The false rate of pile-up identification as a function of the pulse amplitude. (b) The efficiency of the pile-up identification as a function of the first- and the second-pulse amplitudes over an amplitudes ratio of 500 ranging from 7.6 mV to 3.8 V.

I and the pulse Amplitude A, defined as the I/A ratio, does not depend on the pulse amplitude. However, in the case of pile-up the pulse shape is distorted, and the I/A ratio increases. This effect is used for the pile-up pulse identification by monitoring the I/A ratio for the incoming pulses.

Simulations were done to study the performance of the pile-up identification method. The simulation technique is described in section 3.3.1. The I/A ratio as function of the pulse amplitude for single pulses only and for pile-up pulses is shown in figure 6 (a) and (b), respectively. For single pulses, the I/A ratio is almost constant around 14.3, except for the very low pulse amplitudes close to the detection threshold. To calculate the pulse integral, all samples above the threshold are summed up. This simple and fast method of the pulse-integral estimation yields a precise result only for pulses with amplitude much higher than the threshold. In the low-amplitude region the method underestimates the pulse integral. Therefore, as can be noticed in figure 6 (a), the I/A ratio in the low-amplitude region drops below the constant value. However, as shown in figure 6 (b), the I/A ratio for pile-up pulses is larger than observed for a single pulse. Therefore, the pile-up identification is achieved by setting a discriminating threshold $T_{I/A}$ on the I/A ratio. For the investigated pulse shape the optimal threshold value $T_{I/A} = 14.3$ was found. This threshold value is indicated

2012 JINST 7 P11001

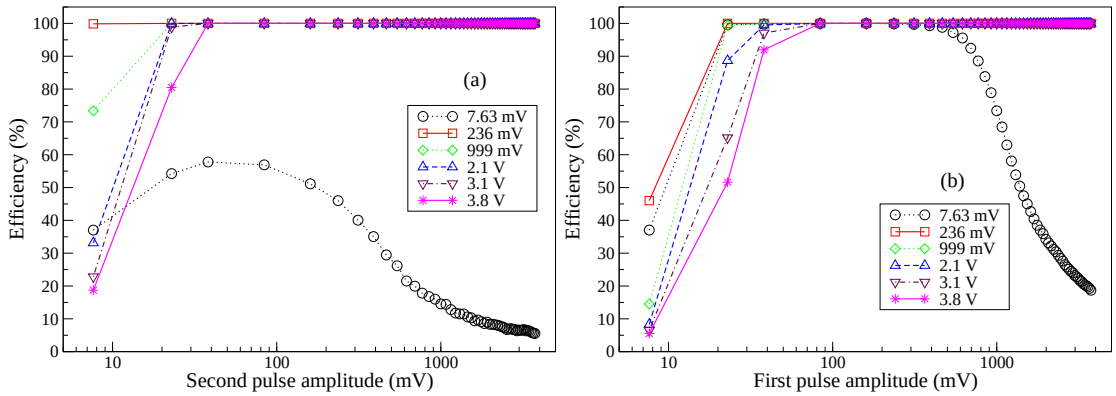

Figure 8. Pile-up identification efficiency as a function of: (a) the second-pulse amplitude for various values of the first-pulse amplitude; (b) the first-pulse amplitude for various values of the second-pulse amplitude. Note the logarithmic horizontal axis.

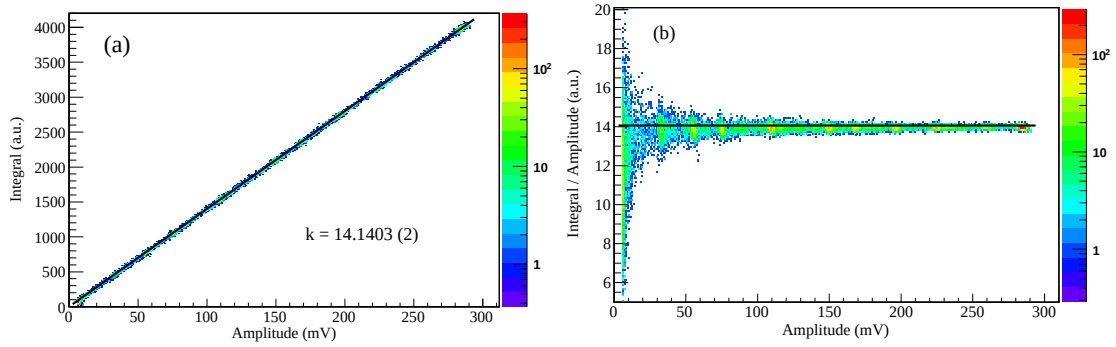

Figure 9. The pulse integral (a) and the ratio of the pulse integral over the pulse amplitude (b) as function of the pulse amplitude obtained for single pulses using the LED light pulser. The linear relationship between the integral and amplitude of a pulse indicates that the pulse shape is stable for different pulse amplitudes.

as horizontal line in figure 6 (a) and (b) and yields a false pile-up identification rate below 1%. The false rate is obtained by simulating single pulses of different amplitudes and counting the fraction of pulses above the I/A threshold. The obtained false pile-up identification rate as function of the pulse amplitude ranging from 7.6 mV to 3.8 V is shown in figure 7 (a). The fraction of pulses above the I/A threshold in figure 6 (b) is defined as the pile-up identification efficiency. The obtained efficiencies as function of the first and the second pulse amplitude are shown in figure 7 (b). Figure 8 shows corresponding slices of the efficiency distribution: (a) for various fixed first-pulse amplitudes and (b) for various fixed second-pulse amplitudes. The detection efficiency is almost 100% for the high-amplitude combinations of pile-up pulses. The efficiency decreases only if one of the pile-up pulse amplitudes approaches the pulse-detection threshold. Therefore, we may conclude that the described pile-up detection algorithm is sufficiently robust and efficient. Moreover, due to its simplicity, the algorithm will consume only little resources in the digitizer FPGA.

2012 JINST 7 P11001

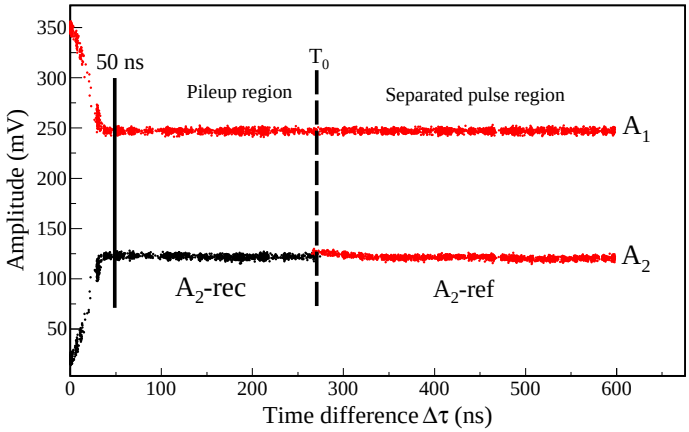

Figure 10. Pulse amplitudes versus the time difference ($\Delta\tau$) for the amplitude ratio 2. Two regions are defined using the time $T_0 = 280$ ns: $\Delta\tau < T_0$ (pile-up pulse region) and $\Delta\tau > T_0$ (separated-pulse region). The dark black data points indicate the recovered second pulse (A_2-rec.). The A_2-rec. amplitude is recovered down to a minimum time difference of 50 ns. The recovery is limited by the time-constant of the shaper.

3.2 Energy recovery

Measurements with a single LED light pulser were performed in order confirm the pulse-shape stability. We measured a linear relation between the pulse amplitude (A) and the pulse integral (I_{single}), i.e., $I_{single} = k \cdot A$, where k is a calibration constant. The distributions of the pulse integral and the I/A ratio as function of the pulse amplitude for single pulses are shown in figure 9 (a) and (b), respectively. Since there are no significant deviations of the I/A ratio from a constant value the pulse shape is obviously stable for various pulse amplitudes. In case of two close events, it is possible to measure the first pulse amplitude (A_1) and the integral (I_{tot}) of the pile-up pulse structure, which contains the energy information of both pulses. Thus, the relation between amplitude and integral is given by $I_{tot} = k(A_1 + A_2)$, which implies $A_2 = (I_{tot}/k) - A_1$, where A_2 is the second pulse amplitude, see figure 4. In figure 10, as an example, the amplitudes of the first and the second pulses are plotted as function of the reference time difference ($\Delta\tau = t_2 - t_1$) between the first and the second pulses, calculated for the amplitude ratio 2. Two regions are defined by the time T_0 = 280 ns (black dashed line): $\Delta\tau < T_0$ is pile-up pulse region and $\Delta\tau > T_0$ is the separated-pulses region. In this second region, the amplitudes shown on the vertical axis are found to be constant (horizontal straight lines) and independent of the time difference. In the region below 50 ns the amplitudes are not constant, since in this region both the pulses overlap completely and appear like a single pulse. In the pile-up region, the second pulse amplitude (black data points) is recovered down to a time difference of 50 ns and the recovered amplitude is constant. The recovery of the second pulse amplitude is limited by the pulse rise time of 50 ns. The pile-up rate for the forward endcap EMC, estimated using a Poisson distribution function is about 13% for the pulse width of 280 ns as found in section 2. Since the pile-up pulse amplitude is recovered down to a time difference of 50 ns, the pile-up rate is reduced to 2.4%, which is close to the PANDA EMC requirement of about 1% [3].

The projections onto the vertical axis of figure 10 for $\Delta\tau > 50$ ns are shown in figure 11 (a) and (b). Figure 11 (a) shows the projection over the time interval of $\Delta\tau > T_0$, the region where

2012 JINST 7 P11001

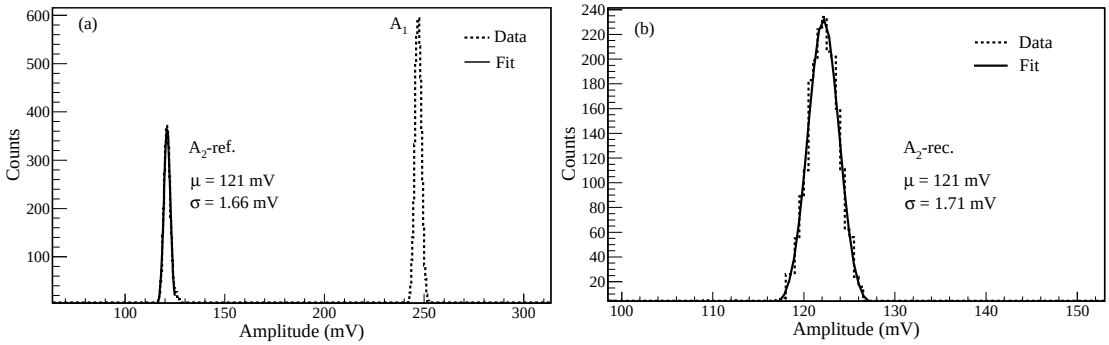

Figure 11. The amplitude distributions obtained projecting onto the vertical axis shown in figure 7: (a) $\Delta\tau > T_0 = 280$ ns, the region of well-separated pulses i.e. the reference pulse amplitude (A_2-ref.). (b) 50 ns $< \Delta\tau < T_0$, the pile-up region, where the second pulse amplitude (A_2-rec.) is obtained by the recovery method. The dashed black-line histogram corresponds to the measured data and the solid black-line to the Gaussian fit.

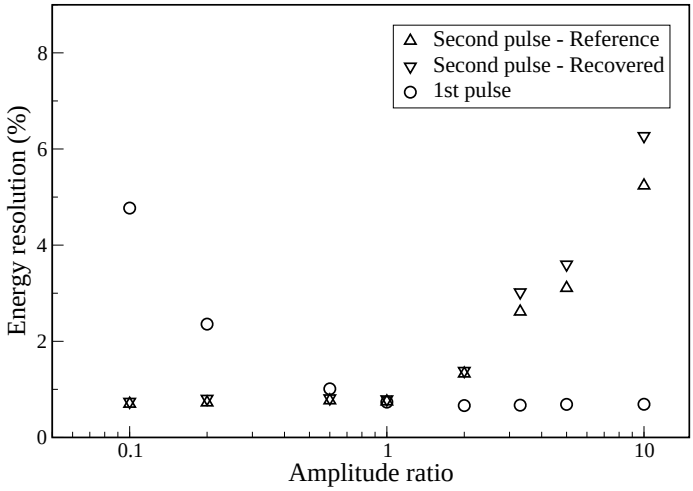

Figure 12. The relative energy resolution σ/μ averaged over a range of time differences is shown as a function of the amplitude ratio. The amplitude ratio of 10 corresponds to a first-pulse amplitude of 250 mV and a second-pulse amplitude of 25 mV. The up-triangle, down-triangle, and circle data points indicate the measured energy resolution for the second reference pulse, the second recovered pulse, and the first pulse, respectively.

pulses are well separated, to obtain the reference resolution for the second pulse. Figure 11 (b) shows the projection over the time interval of 50 ns $< \Delta\tau < T_0$, to obtain the amplitude value and resolution, measured after the recovery procedure. A complete pile-up pulse amplitude recovery is achieved if the recovered pulse amplitude coincides with the reference measurement. The relative energy resolution σ/μ, measured in % is obtained using a Gaussian fit to both the amplitude distributions. The measured reference energy resolution is 1.37% and the recovered resolution is 1.41%. This difference in the resolution is mainly caused by the error propagation of the first-pulse amplitude measurement into the determination of the second-pulse amplitude. We thus note that for a time difference larger than 50 ns the second pulse amplitude can be fully recovered within 1% .

2012 JINST 7 P11001

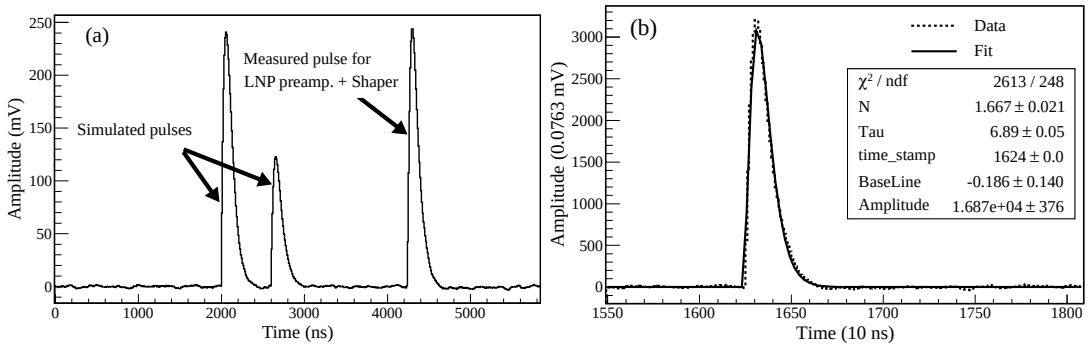

Figure 13. (a) The two pulses introduced by the simulation and the single pulse measured after the LNP + shaper. (b) The single LNP + shaper pulse fitted using equation (1). The pulse amplitude is defined by the parameters Amplitude (A) and N as $A\,e^{-N}$.

The same procedure described above, is followed to study the pulse-amplitude recovery for various amplitude ratios (A_1/A_2). The relative energy resolution σ/μ averaged over a range of time differences $\Delta\tau$ is plotted as function of amplitude ratios in figure 12. The circles indicate the resolution values of the first pulse. The reference resolution (up triangle) averaged over an interval of time differences with $\Delta\tau > T_0$ is compared to the recovered resolution (down triangle) averaged over an interval of time differences with 50 ns $< \Delta\tau <$ T_0. The maximum deviation in resolution is seen for high amplitude ratios, while for low pulse-amplitude ratios the deviation is lower.

3.3 Simulation studies for energy recovery

3.3.1 Single-crystal detector pulse pile-up

In order to test the performance of the energy recovery method for combinations of signals in a wide range of pulse heights, we have simulated special test waveforms. We used the function shown in equation (3.1), which describes the measured pulse shape:

$$f(x) = A\left(\frac{x-t}{\tau}\right)^{N} e^{-N\left(\frac{x-t}{\tau}\right)} + Bl \tag{3.1}$$

Here, the pulse amplitude is obtained as $A\,e^{-N}$ from the parameters A and N, Bl is the baseline, τ is the decay time, and t is the time stamp. The single pulse shape shown in figure 13 (b) was fitted using equation (3.1). This function was used to introduce two additional pulses into the measured signal trace with a time difference chosen in an interval of 50 ns $< \Delta\tau <$ 280 ns. In this way, we can control precisely the amplitude values of the simulated pulses, preserving the realistic noise of the measured waveforms. An example of the simulated pulse is shown in figure 13 (a).

The simulated waveforms were analyzed by following the same procedure used for the measured data. The recovered second-pulse energy resolution σ/μ plotted as function of amplitude of the first and the second pulse is shown in figure 14. In the shown coordinate system, the x-axis is the first-pulse amplitude, the y-axis is the second-pulse amplitude, and the z-axis is the energy resolution obtained for the second pulse. The energy resolution improves as function of the second-pulse amplitude. The relative difference $[(\sigma_{\mathrm{rec}} - \sigma_{\mathrm{ref}})/\sigma_{\mathrm{ref}}]$ between the recovered (σ_{rec}) and reference (σ_{ref}) energy resolution as function of amplitude of the first and second pulse is shown

2012 JINST 7 P11001

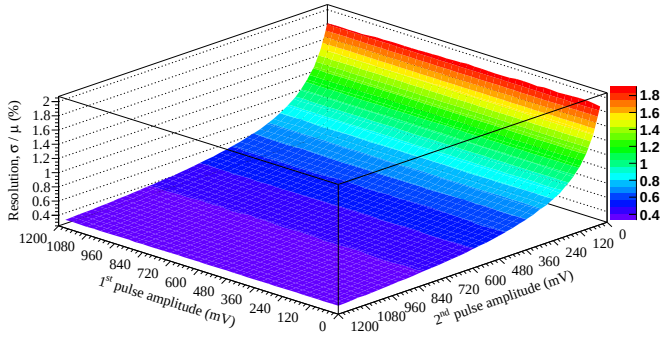

Figure 14. The recovered second-pulse energy resolution (σ / μ) as function of amplitude of the first and the second pulse.

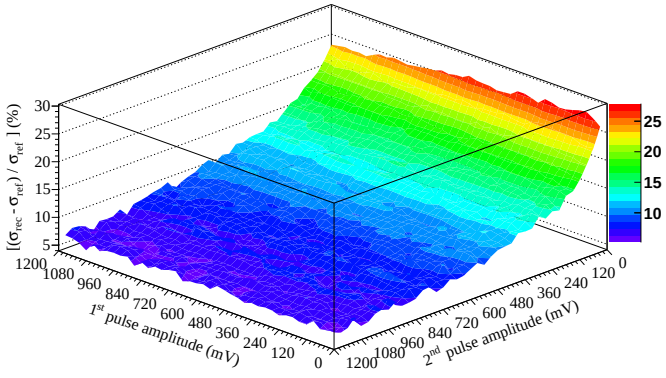

Figure 15. The relative difference $[(\sigma_{\rm rec} - \sigma_{\rm ref})/\sigma_{\rm ref}]$ between the recovered ($\sigma_{\rm rec}$) and reference ($\sigma_{\rm ref}$) energy resolution as function of amplitude of the first and second pulse.

in figure 15. The resolutions can be recovered for all investigated combinations of amplitude of the first and second pulse in the range from 70 mV to 1100 mV. The relative difference is almost independent of the first-pulse amplitude at a given second-pulse amplitude and it is inversely proportional to the second-pulse amplitude. The maximum deviation is seen at the lowest pulse amplitudes, while at higher amplitude values less deviation is obtained. Since the PANDA EMC will be operated in a large dynamic energy range of up to 10000, the equivalent graph of relative differences in resolutions as function of amplitude of the first and the second pulse over a large dynamic amplitude range of 1000 (3.8 V/3.8 mV) is shown in figure 16. The relative difference plotted on the vertical axis follows the same trend over the large dynamic range as seen in figure 15. Once again, the maximum deviation is seen at the lowest pulse amplitudes. The relative difference decreases with the increase in pulse height. Therefore, the results obtained in the investigated dynamic range of 1000 may be safely used as upper limits for the required larger dynamic range of 10000.

2012 JINST 7 P11001

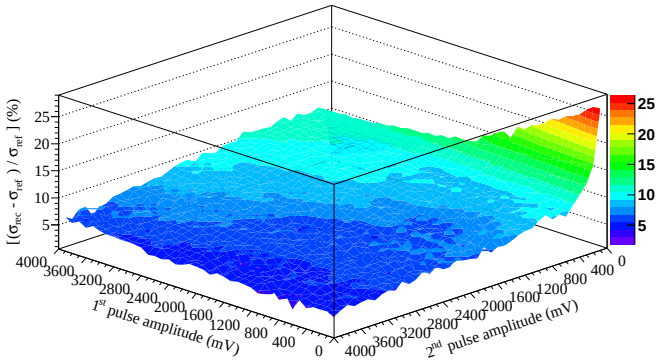

Figure 16. The relative difference $[(\sigma_{\text{rec}} - \sigma_{\text{ref}})/\sigma_{\text{ref}}]$ between the recovered (σ_{rec}) and reference (σ_{ref}) energy resolution as function of amplitude of the first and second pulse over the large dynamic range of 1000 (3.8 V/3.8 mV).

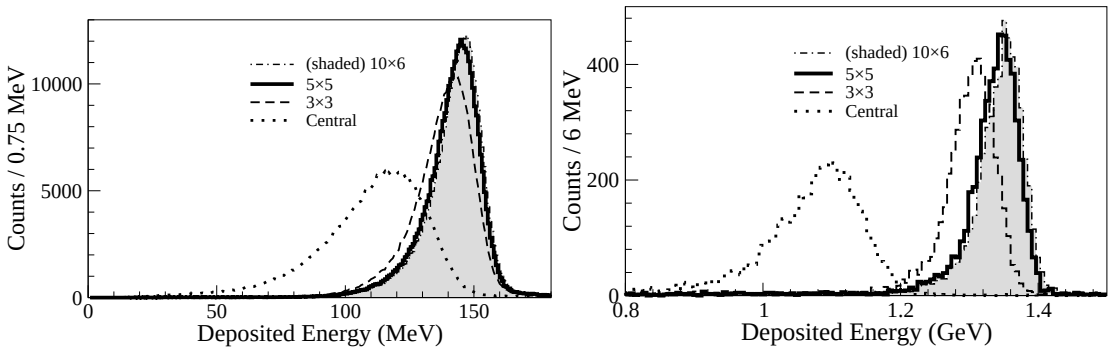

Figure 17. Photon energy deposition spectrum for incident photon energies of 150 MeV (right) and 1.4 GeV (left), obtained with the charge-integrating (QDC) readout of the sixty-crystal EMC prototype (proto60) [12] experiment. The energy depositions in the central crystal and the 3×3, 5×5, and 10×6 crystal matrices are indicated by the dotted line, the dashed line, the solid line and the shaded area, respectively.

3.3.2 Pulse pile-up for 5×5 cluster

To simulate pulse pile-up in a cluster of twenty five scintillating crystals (5×5), that may respond to a single high-energy photon, we have used analysis results obtained with the charge-integrating (QDC) readout of the sixty-crystal EMC prototype (proto60) [12] experiment. In the proto60 experiment, the energy-tagged photons were used to study the detector response. Two examples of the photon energy deposition spectrum are shown in figure 17 (a) and (b) [12] for incident photon energies of 150 MeV and 1.4 GeV, respectively. According to figure 17, we observe 80% of the incident photon energy deposition in the central crystal, 15% in the first ring, i.e. the eight neighboring crystals of the central crystal, and 5% in the second ring, i.e. the sixteen neighboring crystals of the first ring excluding the central crystal. These results were considered while introducing two additional pulses into the measured trace digitized by the SADC. These pulses were generated using the response function shown in equation (3.1) and fed into the measured trace over a time difference interval of 50 ns $< \Delta\tau <$ 280 ns (figure 10) for all detectors in the 5×5 cluster. Using

2012 JINST 7 P11001

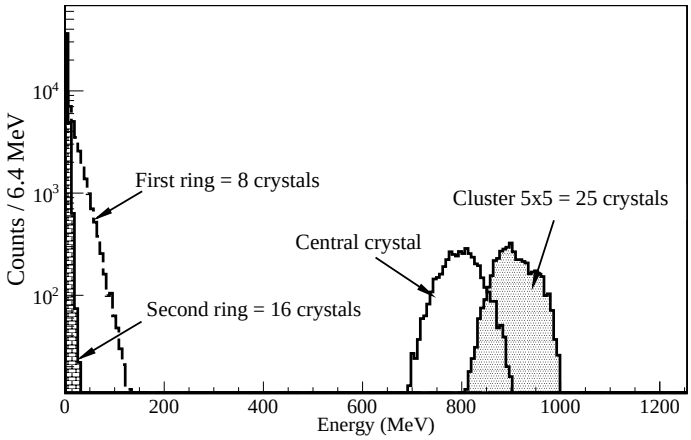

Figure 18. Simulated 5×5 cluster energy deposition spectrum for single pulses at 1 GeV photon energy. The energy depositions in the central crystal, the first ring of crystals, the second ring, and 5×5 crystal matrix are indicated by the solid line, the dashed line, the shaded area with bricks and the shaded area with dots, respectively.

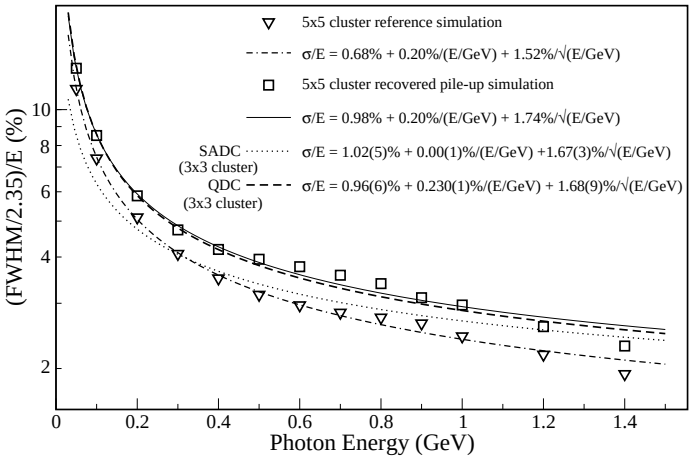

Figure 19. Energy resolution for the pile-up recovered second-pulse as function of photon energy. The triangles are the reference resolution for the 5×5 cluster and the dash-dot line is the corresponding fit. The squares are the pile-up recovered resolution for 5×5 clusters and the solid line is the corresponding fit. The dashed line is the 3×3 cluster resolution for QDC readout and the dotted line is the 3×3 cluster resolution for SADC readout (data from [12]).

the measured first-pulse signal has the advantage that the proper electronic noise is included in the pile-up simulation. The simulated 5×5 cluster energy-deposition spectrum is shown in figure 18. To study the energy recovery of pile-up pulses over the cluster, the simulations were done for various photon energies ranging from 50 MeV to 1.4 GeV of the second pulse while the first-pulse energy was about 300 MeV. The 5×5 cluster energy spectrum was fitted using an asymmetric Gaussian fit function [13] to obtain the peak position and Full Width at Half Maximum (FWHM). The energy resolution as function of the photon energy is shown in figure 19. The energy resolution is defined as (FWHM/2.35)/(peak position). The 5×5 cluster simulation produces an energy reso-

2012 JINST 7 P11001

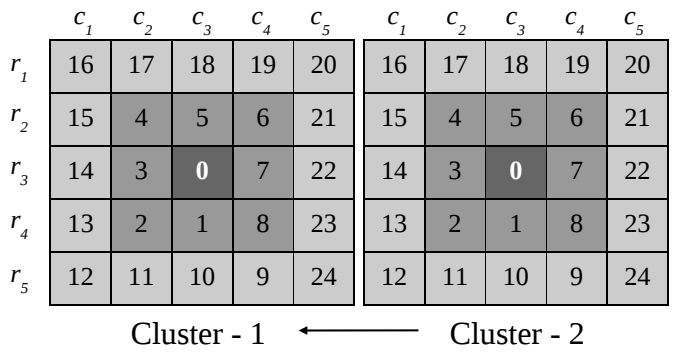

Figure 20. Schematic representation of two symmetric 5×5 clusters. The letters c_1, c_2, c_3, c_4, and c_5 indicate the columns and r_1, r_2, r_3, r_4, and r_5 indicate the rows of the symmetric 5×5 cluster.

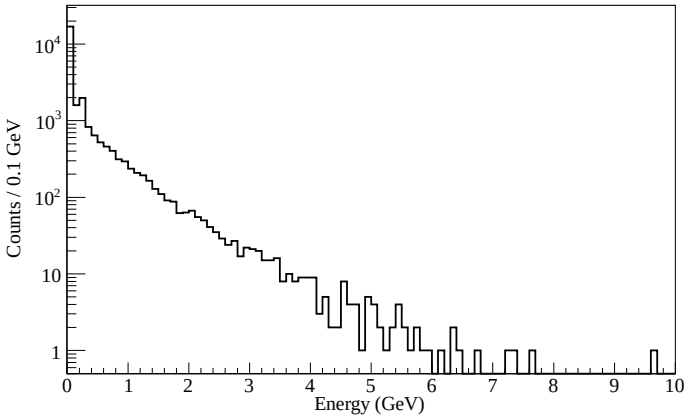

Figure 21. The photon energy distribution for the forward endcap PANDA EMC simulated using the DPM (Dual Parton Model) background generator at $\bar{p}$ beam momentum of 15 GeV.

lution close to the values obtained for proto60 [12]. The reference 5×5 cluster energy resolution shows slightly better resolution values than the 3×3 cluster SADC data because of the 5×5 cluster summation. The pile-up recovered cluster energy resolution is 20% worse than the non-pile-up cluster energy resolution.

3.3.3 Pulse pile-up for two overlapping 5×5 clusters

In order to determine the impact of pile-up recovery on the effective energy resolution, we studied overlapping clusters of photons and the probabilities for certain overlap situations. To generate pulse pile-up in the overlapping regions of two neighboring clusters, two symmetric 5×5 clusters were simulated as described in the previous section. These two clusters were named cluster-1 and cluster-2 as shown in figure 20. The crystal marked by 0 in both the clusters receives the highest energy deposition in comparison with its neighboring crystals and hence it is called "seed". The photon energy distribution for the forward endcap EMC was simulated using the DPM (Dual Parton Model) background generator [14] embedded in the PandaRoot software package [15]. In the DPM generator, $p\bar{p}$ inelastic scattering produces a parton shower forming resonances (π^0, η, Δ, Σ, etc.) which further decay within the volume of the detector. The simulated photon energy distribution shown in figure 21 was used as input for the energy deposition in cluster-1. The input energy

2012 JINST 7 P11001

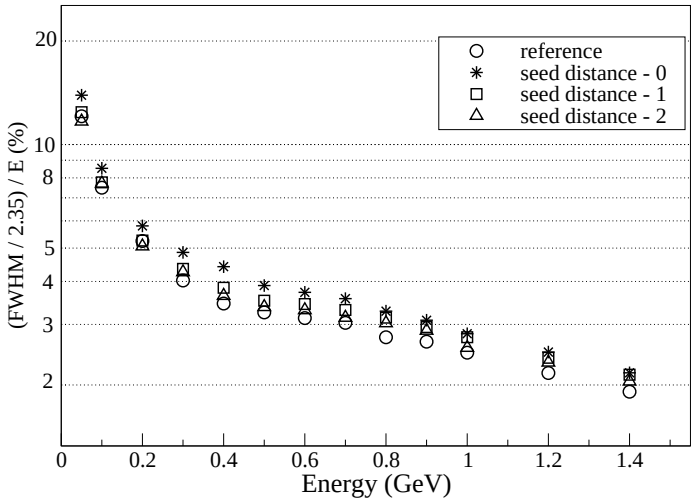

Figure 22. Energy resolution for the pile-up recovered second pulse as function of the energy. The circles indicate the reference energy resolution for 5×5 cluster without any overlap or pile-up. The seed distance-2 (triangles), seed distance-1 (squares), and seed distance-0 (stars) indicates the pile-up recovered second-pulse energy resolution for the overlapping columns of both the showers.

deposition for cluster-2 was varied from 50 MeV to 1.4 GeV at time differences relative to cluster-1 randomly chosen from 50 ns to 280 ns and the pile-up pulses were simulated in the overlapping regions of 5×5 clusters.

To simulate overlapping regions where the pulse pile-up will occur, clusters-2 was moved in steps of one column in the direction of the arrow towards cluster-1 (see figure 20). If the first column (c_1) of cluster-2 overlaps the last i.e. the fifth column (c_5) of cluster-1, the distance between the seeds of cluster-1 and cluster-2 is four crystals and hence this situation is called "seed distance-4 ($s.d.4$)". Accordingly, the overlapping situations for the remaining four columns were defined as "seed distance-n ($s.d.n$)", $n = 0$ to 3, with $n = 0$ for complete overlap. The energy resolution for the pile-up recovered second pulse as function of the energy is shown in figure 22. The pile-up recovered energy resolution for the seed distance-3 and 4 produces energy resolutions almost equal to the reference energy resolution. The relative difference between the reference energy resolution and the recovered energy resolution for seed distance-0 is about 20%. In the simulation above, we have considered the worst-case scenario in which the two 5×5 clusters were shifted against each other in the horizontal direction. In this way we obtained the largest overlap of single-crystal hits for a particular seed distance. Therefore, the presented simulation provides a conservative estimate of the pile-up effect on the final performance of the EMC.

The geometry of the forward endcap EMC was taken into account to estimate the overlap-occurrence probabilities of the five selected cases. In order to obtain a worst-case estimate, we chose the region of highest hit rates with polar angle θ between 5° and 10° (see figure 1). The probability of a second photon hitting a certain position in the overlap region is proportional to $P_{(s.d.n)} = P_{r_i(c_i+c_j-1)}(\theta_i)$, where i and j ($1 \leq i,\ j \leq 5$) are the hit position indices of cluster-1 and cluster-2, respectively, generating overlap at five representative seed distances. For a fixed seed distance the hit probability for each relevant crystal depends on the polar angle. The probability $P_{r_i c_i}(\theta_i) \sim \left(\frac{1}{N(\theta_i)}\right)$, where $N(\theta)$ is the number of crystals located at the polar angle θ.

2012 JINST 7 P11001

We assume that the first photon hits the EMC at a fixed position c_3 r_3 (see figure 20) in one of the 5×5 clusters with probability proportional to $P_{r_3c_3}$. The probability of a second photon hitting one of the nearest neighbors for the case of seed distance-1 ($s.d.1$) is defined by $P_{(s.d.1)}$:

$$P_{(s.d.1)} = \sum_{i=2,4} P_{r_3c_i} + \sum_{i=2}^{4} (P_{r_4c_i} + P_{r_2c_i}) \tag{3.2}$$

Similarly, the probabilities of a second photon hitting in the vicinity of the first hit for the other cases were evaluated. The resulting normalized overlap probabilities for the case $s.d.0$ to $s.d.4$, exhausting all possible worst-case pile-up cases, are 1%, 9%, 19%, 30%, and 41%, respectively. Hence the probability of complete shower overlap ($s.d.0$) is almost negligible compared to the peripheral overlap ($s.d.3$ or $s.d.4$).

In the peripheral overlap region the pile-up of low-energy pulses will occur. According to figure 15 the maximum difference between the pile-up recovered and the reference energy resolution was seen at the lowest pulse amplitudes. However, the effective energy resolution for a 5×5 cluster for peripheral overlap including the slight deterioration due to the pile-up recovery, is almost not affected. The resulting energy resolution for the endcap obtained by averaging the properly weighted energy resolutions shown in figure 22, only slightly deteriorates. For example, the pile-up free energy resolution at 1 GeV is 2.48%, the effective energy resolutions for EMC hit rates of 1 MHz and 500 kHz are 2.50% and 2.49%, respectively.

3.4 Time recovery

The time stamp of the pulse was estimated using the Constant Fraction Timing (CFT) method [12]. This is realized using an algorithm that is described by equation (3.4). In this method, a fraction f of the pulse amplitude is inverted and added to the pulse, after being delayed by the rise time of the pulse.

$$I[i] = -f\,(S[i] - Bl) \tag{3.3}$$

$$CFT[i] = I[i] + (S[i - D] - Bl) \tag{3.4}$$

In equation (3.4), $I[i]$ is the attenuated and inverted pulse amplitude for sample i, f is the attenuation constant or fraction of the pulse amplitude, $S[i]$ is the raw digitized data at sample i, Bl is the baseline, $CFT[i]$ is the CFT signal, and D is the time delay. The CFT algorithm was applied at the leading edge to obtain the time stamp t_1 of the first pulse. Equivalently, to obtain the time t_2 of the second pulse, the CFT algorithm was applied at the trailing edge. This approach implies using measured data in the time-reversed order to obtain t_2. An example of a digitized raw pulse and the CFT signal is shown in figure 23 (a) and (b), respectively. in figure 23 (b) the linear interpolation (solid line) was applied to estimate the zero-crossing point (dashed line), which defines the time-stamp of the second pulse.

The time difference between trailing and leading edge is defined as the *recovered* time difference ($\Delta\, T$). In order to characterize the performance of the algorithm we introduce a reference time difference ($\Delta\tau$). It is known only for the performed simulations and validation experiment (see section 2). The subtraction of the reference time difference ($\Delta\tau$) from the recovered time difference ($\Delta\, T$) results in the difference ($\Delta\, T - \Delta\tau$) which is equivalent to the pulse width and

2012 JINST 7 P11001

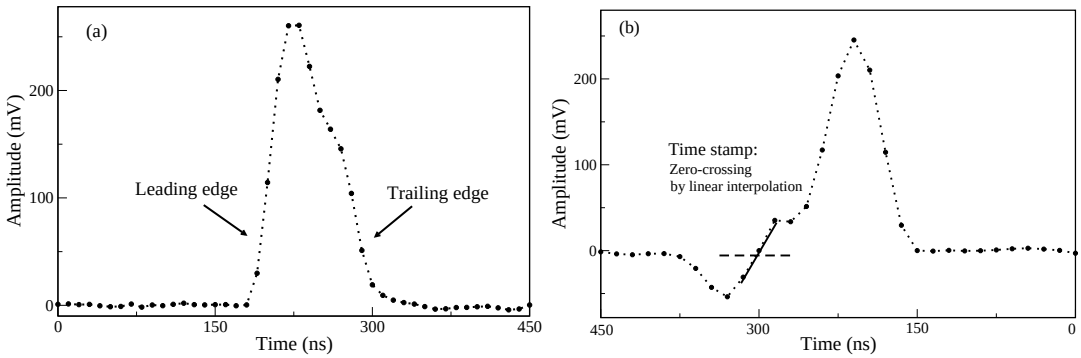

Figure 23. (a) An example of a digitized pile-up pulse. (b) CFT signal constructed using the time-inverted data to extract the trailing edge timing for the second pulse in the pile-up structure. A linear interpolation was applied to find the zero-crossing point which defines the time stamp of the second pulse.

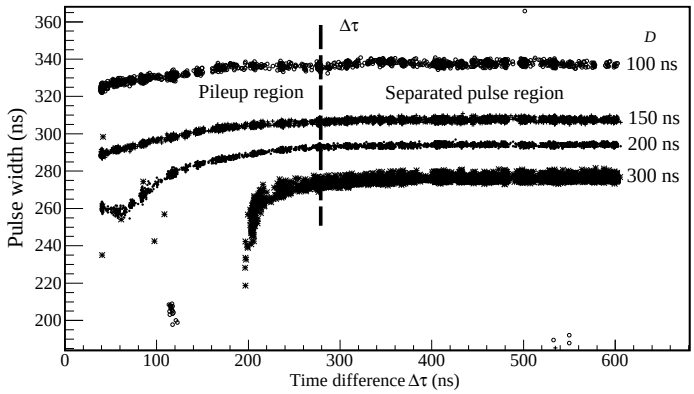

Figure 24. The pulse width ($\Delta\, T - \Delta\tau$) versus time difference $\Delta\tau$ for different values of the CFT time delay parameter D for an amplitude ratio 2. The region $\Delta\tau\ < 280$ ns is the pile-up region where the pulse width is not constant due to the asymmetric pile-up pulse shape.

is expected to be constant because the pulse shape was found to be constant. The obtained pulse width as function of $\Delta\tau$ for different values of the CFT parameter time delay D is shown in figure 24. In the region $\Delta\tau > 280$ ns the pulse width is constant as expected for a well separated pulse. The region $\Delta\tau < 280$ ns is the pile-up region where the measured pulse width is not constant due to the overlap of the second pulse at the trailing edge of the first pulse. This resulting distortion is amplified by the asymmetric pulse shape. Due to this effect it is almost impossible to recover the time stamp in the pile-up region.

To symmetrize the asymmetric pulse shape, we have applied the Moving Window Deconvolution (MWD) [16, 17] filter on the digitized raw pulse. The MWD filter is expressed in equation (3.5).

$$MWD_M(n) = x(n) - x(n-M) + \frac{1}{\tau}\sum_{i=n-M}^{n-1} x(i), \tag{3.5}$$

where M is the length of the filter, τ is the decay time of the signal, and $x(n)$ is the n^{th} input sample. The MWD filter differentiates the raw signal with the length (M) of the filter and compensates for the exponential decay of the signal using the decay time τ. Thus, the MWD filter cancels the

2012 JINST 7 P11001

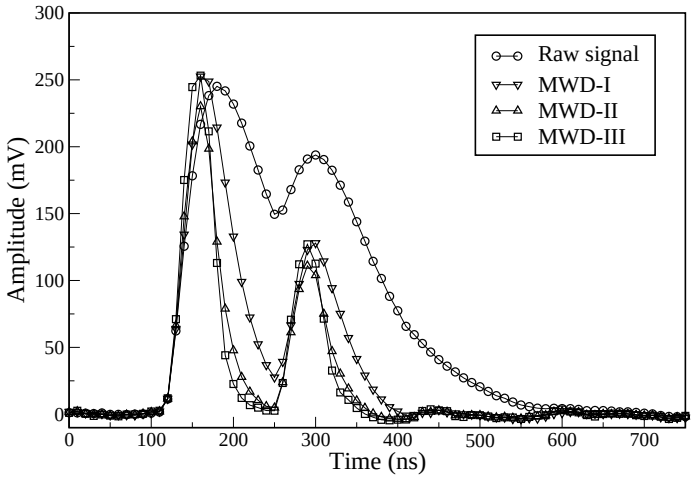

Figure 25. The comparison of the raw digitized and MWD filtered pulse shapes. Circles: raw pulse shape at $\Delta\tau = 100$ ns for the amplitude ratio 2, triangles down: MWD applied once (MWD-I), triangles up: MWD applied twice (MWD-II), squares: MWD applied three-times (MWD-III). After MWD-III, the pile-up pulses appear as two separated single pulses with a more symmetric shape.

semi-exponential tail of the shaped pulse. The resulting pulse shape is shown in figure 25. A single MWD filtering can not completely compensate the tail of the pulse, as it does not have the perfect exponential behavior. After applying the MWD filter two times, the tail at the trailing edge is still visible. Hence we have applied the MWD filter three times (MWD-III) in order to obtain pile-up pulses appearing as two separated single pulses with a symmetric shape. The pulses obtained after the MWD-III filter were used to apply the time recovery algorithm. The corresponding filter parameters are shown in table 1. For each MWD filter the parameter M was chosen to be slightly larger than the pulse width in order not to affect the pulse amplitude. The values of the decay-time parameter τ were deduced from the exponential fit of the trailing edges of the pulses at each filtering step. The same pulse shape can be achieved by different combination of M and τ parameters. A selection of a particular combination of the parameters does not influence the performance of the recovery-algorithm described below, since the performance depends only on the resulting pulse shape. Since the pulse shape is symmetric, we expect the measured pulse width ($\Delta\, T - \Delta\tau$) to be constant. The resulting distribution of the pulse width as function of $\Delta\tau$ is shown in figure 26 (a). The pulse width obtained is constant above $\Delta\tau = 10$ ns. The projection onto the vertical axis of figure 26 (a) is shown in figure 26 (b). The uncertainty (σ) of the pulse-width distribution is defined as the time resolution for the pile-up pulses. The obtained average time resolution is ~ 1 ns for the amplitude ratio 2. The same procedure is repeated for various amplitude ratios (first-pulse amplitude / second-pulse amplitude). The result of the averaged time resolution as function of the amplitude ratio is shown in figure 27. The reference pulse resolution (triangles) is compared with the recovered pulse resolution (circles). The maximum deterioration of the time resolution is about a factor 2.

The effect of the MWD filter on the energy resolution is shown in figure 28, obtained for a single simulated pulse amplitude of 250 mV. The energy resolution gets worse due to the application of the MWD filter onto the digitized signal. Thus, the MWD filter will not be used for energy recovery of pile-up pulses.

2012 JINST 7 P11001

Table 1. The MWD parameter values used to generate symmetric pulse shapes.

Parameter	Filter type		
	MWD-I	MWD-II	MWD-III
M (ns)	40	20	20
τ (ns)	80	30	20

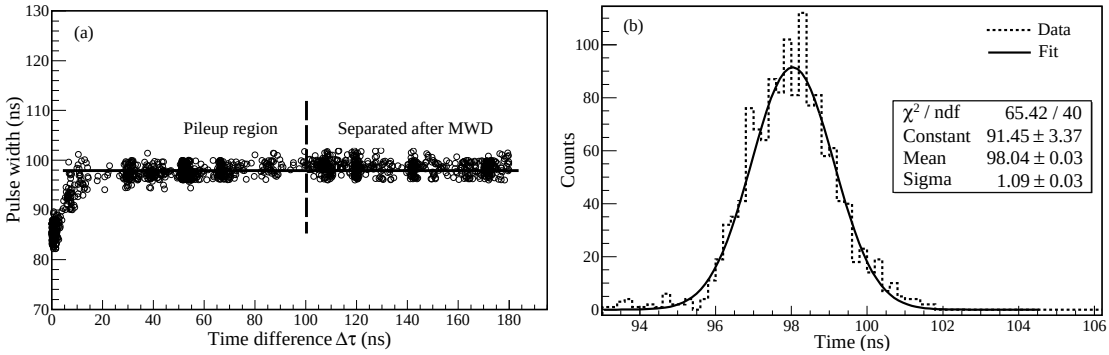

Figure 26. (a): The pulse width ($\Delta\ T - \Delta\tau$) versus time difference $\Delta\tau$. The pulse width is constant (solid horizontal line) above $\Delta\tau = 10$ ns. The vertical dashed line separates the pile-up region from the region where pulses are separated after the MWD filter. (b): The projection onto the vertical axis of figure (a). The pulse-width distribution is fitted with a Gaussian function (solid line). The obtained uncertainty (σ) or the average time resolution is ~ 1 ns for the amplitude ratio 2.

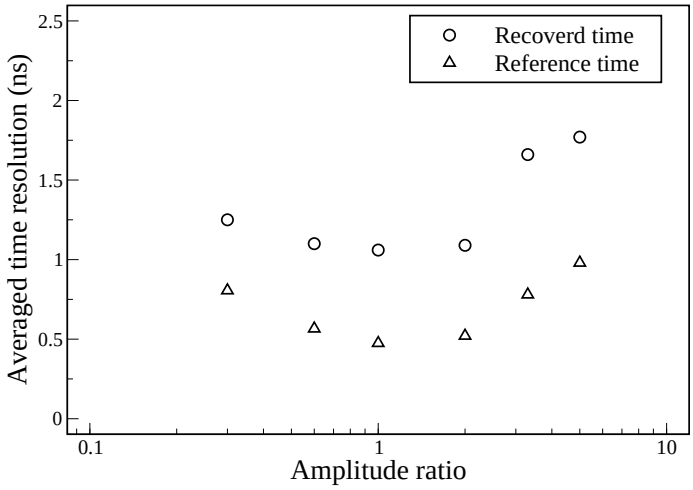

Figure 27. The comparison of the averaged time resolution of the recovered (circles) and the reference pulse (triangles) as function of the amplitude ratio. The amplitude ratio of 2 corresponds to a first-pulse amplitude of 250 mV and a second-pulse amplitude of 125 mV. Significant time recovery is obtained.

3.5 Simulation studies for time recovery

Simulations were done to study the performance of the time recovery method over a large dynamic energy range. The procedure described in section 3.3 was followed to generate pile-up pulses. However, in the wide dynamic amplitude range the pile-up region with full recovery of the pulse

2012 JINST 7 P11001

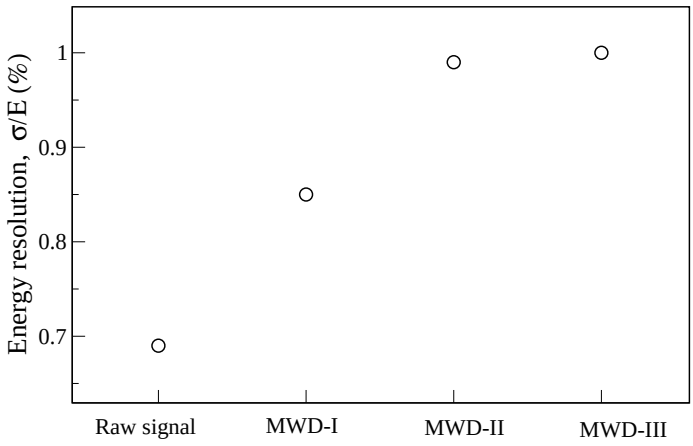

Figure 28. The energy resolution obtained for a single simulated pulse amplitude of 250 mV as function of the signal type without filter (raw) or after the MWD filter of level I to III.

width (see figure 26) is limited to time differences $\Delta\tau >$ 50 ns because otherwise the second pulse, after the MWD filter, can not be safely separated for all amplitude combinations.

Equation (3.1) was used to introduce two additional pulses into the measured signal trace with a time difference chosen in an interval of 50 ns $< \Delta\tau <$ 100 ns. The time recovery method has been described in the previous section where the MWD-III filter was used to obtain a symmetric pulse shape as seen in figure 25. Due to the MWD-III filter the pulse width was reduced to $\sim$ 100 ns. Thus the maximum time difference of 100 ns was used to simulate pulse pile-up. To obtain the time stamp, the CFT method was applied to the leading edge of the first pulse and to the trailing edge of the second pulse in the pile-up structure. The time difference between trailing-edge and leading-edge time stamps is called the *recovered* time difference (section 3.4). The recovered time resolution σ_{rec} as function of the first and the second-pulse amplitude over a large dynamic energy range of $\sim$ 1000 (7 V/7 mV) is shown in figure 29. The recovered time resolution σ_{rec} shown on the vertical axis is obtained from the variance of the time difference distribution obtained by subtracting the recovered time difference and the true time difference. The time resolution improves as function of the second-pulse amplitude.

The same simulation procedure and the time-recovery method have been applied on pulses well separated in time, obtained by adding two pulses with a time difference chosen in an interval of 300 ns $< \Delta\tau <$ 350 ns. The resulting time resolution σ_{ref} is plotted as function of the first and the second-pulse amplitudes in figure 30. The time resolution for well-separated pulses improves as function of both the pulse amplitudes.

The relative difference $[(\sigma_{\text{rec}} - \sigma_{\text{ref}})/\sigma_{\text{ref}}]$ between the recovered (σ_{rec}) and the reference (σ_{ref}) time as function of the first and second-pulse amplitude over a large dynamic range of $\sim$ 1000 (7 V/7 mV) is shown in figure 31. The largest deviation is seen at the lowest second-pulse amplitudes, while at the lowest first-pulse amplitudes a significant time recovery is obtained. The MWD-III filter plays an important role in the region of low amplitudes of the second pulse. If the first-pulse amplitude is very high, e.g. 7 V, and the second-pulse amplitude is very low, e.g. 7 mV, the MWD-III filter is unable to reconstruct the second pulse amplitude, resulting in the

2012 JINST 7 P11001

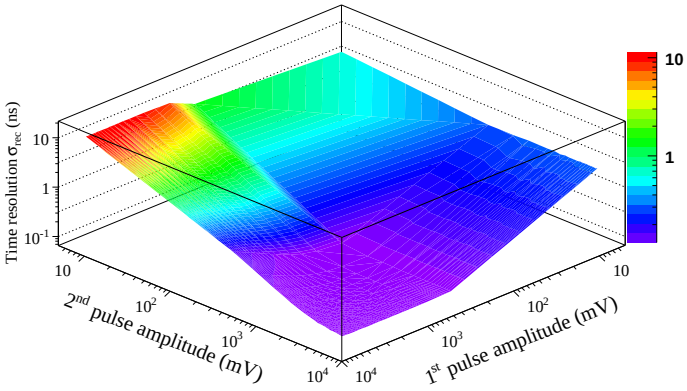

Figure 29. The pile-up recovered time resolution σ_{rec} as function of the first and the second pulse amplitude over a large dynamic range of ~ 1000 (7 V/7 mV).

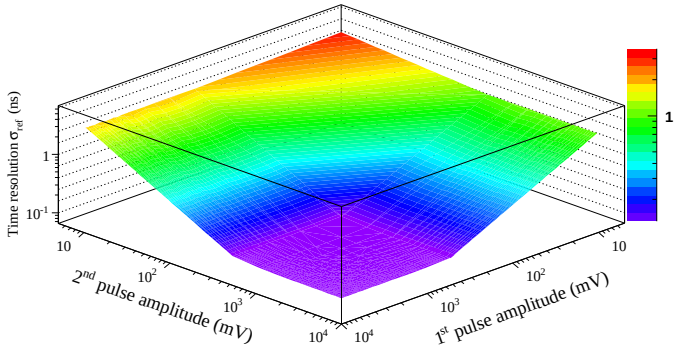

Figure 30. The time resolution σ_{ref} of the well separated pulses as function of the first and the second pulse amplitude over a large dynamic range of ~ 1000 (7 V/7 mV).

maximum deviation in the relative difference. Conversely, if the first-pulse amplitude is low and the second-pulse amplitude is high then the MWD-III filter recovers the second pile-up pulse resulting in smaller deviations and significant time recovery. On the other hand, the maximum deviation in the relative time difference is seen for the higher pulse amplitude ratios (first pulse/second pulse) while less deviation is seen for the lower pulse amplitude ratios.

3.6 Pile-up rate

The pile-up rate was estimated using a Poisson time-distribution function:

$$P[k;(r\times w)] = \frac{(r\times w)^k e^{-(r\times w)}}{k!} \tag{3.6}$$

where r is the hit rate for the EMC, w = 280 ns is the pulse width, k is the number of occurrences of the events within a time interval equal to the pulse width w. The pile-up rate as function of the EMC hit rate is shown in figure 32. The pile-up rate at a hit-response time of 280 ns is rather high and is significantly reduced using the proposed pile-up recovery method by recovering features of

2012 JINST 7 P11001

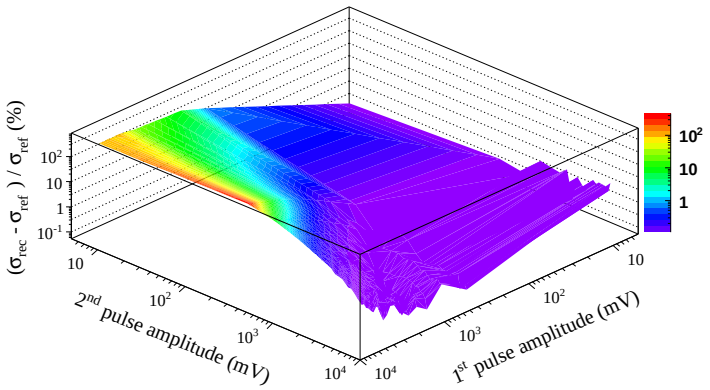

Figure 31. The relative difference $[(\sigma_{rec} - \sigma_{ref})/\sigma_{ref}]$ between the recovered (σ_{rec}) and reference (σ_{ref}) time as function of the first and second pulse amplitude over a large dynamic range of $\sim$ 1000 (7 V/7 mV).

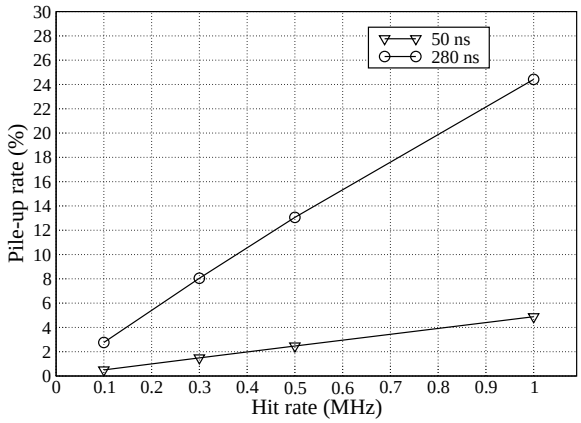

Figure 32. The pile-up rate as function of the EMC hit rate estimated using a Poisson time-distribution function. The circles indicate the pile-up rate at a hit-response time of 280 ns and the triangles indicate the remaining pile-up rate after pile-up recovery for an effective hit-response time of 50 ns.

all pulses arriving after a time delay of about 50 ns. Due to the hydrogen pellet target fluctuations, the most forward region ($\theta = 5^\circ$ to 7°) of the forward endcap EMC will be exposed to a peak hit rate of 1 MHz resulting in a pile-up rate of 24%. After applying the recovery method, the remaining pile-up rate is reduced to 4.2%. Similarly, at hit rates of about 500 kHz the pile-up rate is about 13%. The reported pile-up recovery method can reduced this rate to 2.4%.

4 Summary and outlook

A pulse pile-up recovery method is developed and tested for the front-end electronics of the PANDA EMC. It allows to recover the pulse amplitude completely with a minimum time difference equal to the pulse rise-time. The pile-up rate of 13% is reduced to 2.4%. Pile-up simulations are done to study the energy recovery over a large dynamic energy range of 1000. It is seen that the relative difference in recovered and reference energy resolution is almost independent of the

2012 JINST 7 P11001

first-pulse amplitude and it is inversely proportional to the second-pulse amplitude. The maximum deviation is seen for the lowest pulse amplitudes, while at higher amplitude values less deviation is obtained. The simulation studies for the 5×5 cluster energy recovery reproduces the energy resolution values obtained for the prototype experiment proto60. The pile-up recovered cluster energy resolution is at most 20% worse than the pile-up free cluster energy resolution. Similarly the overlapping-shower simulation studies have shown that the recovered energy resolution for the peripheral overlap produces energy resolutions almost equal to the pile-up free reference energy resolution. The difference between the reference energy resolution and the recovered energy resolution for maximum overlap is about 20%. The estimated probabilities for the occurrence of two overlapping showers vary from 1% to 41% from maximum to peripheral overlap, respectively. The effective energy resolution, obtained by properly weighting the pile-up recovered energy resolutions and the reference energy resolutions for a 5×5 cluster, reveals only little deterioration, e.g., at 1 GeV and for an EMC hit rate of 1 MHz a change from 2.48% to 2.5% is observed.

The CFT method is applied at the trailing edge of the pile-up pulse. The tail at the trailing edge plays an important role in the time recovery. The MWD filter is applied three times to remove the tail at the trailing edge and to obtain a more symmetric pulse shape. Simulations were done to study the time recovery over a wide dynamic range of 1000. The systematic behavior of the observed results allows a safe extrapolation to the required dynamic range of 10000. In the lowest second-pulse amplitude region the MWD-III filter is unable to reconstruct the second pulse amplitude resulting in a large deviation in the relative difference in time resolution. Conversely, in the lowest first-pulse amplitude region the MWD-III filter recovers the second pile-up pulse, resulting in a small deviation and significant recovery of time resolution. The reported method for energy and time recovery is simple and easy to implement in FPGAs.

References

[1] PANDA collaboration, W. Erni et al., *Physics Performance Report for PANDA: strong interaction studies with antiprotons*, arXiv:0903.3905.

[2] P. Spiller and G. Franchetti, *The FAIR accelerator project at GSI*, *Nucl. Instrum. Meth.* **A 561** (2006) 305.

[3] PANDA collaboration, W. Erni et al., *Technical design report for the PANDA electromagnetic calorimeter*, arXiv:0810.1216.

[4] M. Kavatsyuk et al., *Trigger-less readout electronics for the PANDA Electromagnetic Calorimeter*, *IEEE Nucl. Sci. Symp. Conf. Rec.* (2011) 43.

[5] E. Guliyev et al., *VHDL implementation of feature-extraction algorithm for the PANDA electromagnetic calorimeter*, *Nucl. Instrum. Meth.* **A 664** (2012) 22.

[6] M. Vencelj et al., *Event by event pile-up compensation in digital timestamped calorimetry*, *Nucl. Instrum. Meth.* **A 607** (2009) 581.

[7] F. Belli et al., *A method for digital processing of pile-up events in organic scintillators*, *Nucl. Instrum. Meth.* **A 595** (2008) 512.

[8] A. Paul et al., *Maximum likelihood estimation techniques for high rate, high throughput digital pulse processing*, *IEEE Nucl. Sci. Symp. Conf. Rec.* (2008) 1668.

2012 JINST 7 P11001

[9] PANDA collaboration, W. Erni et al., *Technical design report for the PANDA internal targets: the cluster-jet target and developments for the pellet target*, submitted to FAIR (2012).

[10] W. Erni and M. Steinacher, *Struck innovative system — Sampling Analog to Digital (SADC) converter*, in *PANDA technical progress report* (2005), p. 204.

[11] SIS3302 SADC, http://www.struck.de/sis3302.htm.

[12] M. Kavatsyuk et al., *Performance of the prototype of the electromagnetic calorimeter for PANDA*, *Nucl. Instrum. Meth.* **A 648** (2011) 77.

[13] A.R. Gabler et al., *Response of TAPS to monochromatic photons with energies between* 45 *and* 790 *MeV*, *Nucl. Instrum. Meth.* **A 346** (1994) 168.

[14] A. Galoyan and V.V. Uzhinsky, *New Monte Carlo implementation of quark-gluon-string model of $\bar{p}p$-interactions*, *AIP Conf. Proc.* **796** (2005) 79.

[15] PANDA collaboration, J.G. Messchendorp, *Computing activities for the PANDA experiment at FAIR*, *J. Phys. Conf. Ser.* **219** (2010) 042016.

[16] A. Georgiev and W. Gast, *Digital pulse processing in high resolution, high throughput, γ-ray spectroscopy*, *IEEE Trans. Nucl. Sci.* **NS-40** (1993) 770.

[17] J. Stein et al., *X-ray detectors with digitized preamplifiers*, *Nucl. Instrum. Meth.* **B 113** (1996) 141.

2012 JINST 7 P11001